International Journal of Hydrogen Energy 146 (2025) 149987

Contents lists available at ScienceDirect

International Journal of Hydrogen Energy

journal homepage: www.elsevier.com/locate/he

Fullerene nano-confinement enables ultra-low dehydrogenation temperature of MgH_2: A DFT-Based theoretical prediction

Junyi Wo [a,b], Weijie Yang [a,b,*]

[a] Department of Power Engineering, School of Energy, Power and Mechanical Engineering, North China Electric Power University, Baoding, 071003, China
[b] Hebei Key Laboratory of Energy Storage and Integrated Energy Systems, North China Electric Power University, Baoding, 071003, Hebei, China

ARTICLE INFO

Handling Editor: Umit Koylu

Keywords:
Fullerene nanoconfinement
DFT calculation
Dehydrogenation temperature reduction
Linear correlation model

ABSTRACT

Magnesium-based solid-state hydrogen storage boasts high hydrogen density and exceptional safety, yet it frequently encounters hurdles due to sluggish absorption/desorption kinetics and excessive operating temperatures. Currently, the nanoconfinement effect is widely considered a pioneering strategy to overcome these obstacles, thereby directing ongoing research toward the discovery of effective confining materials. However, developing a new nanoconfinement system capable of storing and releasing hydrogen at low temperatures remains a challenge. To address this challenge, we employed density functional theory (DFT) to explore the nanoconfinement effect of fullerene (C_n) on magnesium hydride (MgH_2) nanoparticle clusters. By systematically changing the ratio of particle size to pore size and introducing heteroatom doping (boron and phosphorus), we found that increasing this ratio can improve structural stability, promote the weakening of H–Mg bonds, and enhance interfacial charge transfer, thereby significantly reducing the initial dehydrogenation temperature. Significantly, compared to the observed 102 °C in ordered mesoporous carbon (CMK-3) experiments with the same size ratio, the C_{180} doped with 1.01 wt% B reduces the predicted ultra-low onset dehydrogenation temperature to only 69.26 °C. In addition, all nano constrained structures share the same dehydrogenation temperature linear fitting descriptor *k* value, while the *b* value can be predicted using the single point energy of the carbon-based carrier as a descriptor. These results provide theoretical insights into the structureproperty relationship of nanoconfined MgH_2 and practical strategies for designing efficient hydrogen storage materials under mild conditions.

1. Introduction

Hydrogen, heralded as the most promising secondary energy source of the 21st century, offers a multitude of advantages, such as its high energy content, eco-friendliness, abundant availability, and extensive use [1–3]. It has emerged as a pivotal solution to address challenges in energy storage, smoothing out fluctuations in renewable energy, and spearheading the transition towards a low-carbon future [4–6]. Among the myriad hydrogen storage and transportation technologies, solid-state hydrogen storage distinguishes itself with its high density, safety, and extended storage capabilities [7]. Research endeavors and practical applications in this domain, particularly involving magnesium and carbon-based materials, are progressively advancing [8,9]. However, existing research indicates that magnesium-based hydrogen storage materials exhibit sluggish hydrogen absorption and desorption rates, inadequate reaction kinetics, and a tendency to undergo corrosion when employed as anode materials, resulting in diminished cycling stability. Moreover, the most critical factor limiting their application is the high temperature required for hydrogen liberation [10–12].

Therefore, developing efficient solid-state hydrogen storage materials and technologies is crucial for the practical use of hydrogen energy. Currently, there are several approaches to improving the hydrogen storage and release performance of magnesium hydride (MgH_2), such as spatial nanoconfinement, MgH_2 powder nanonization [13], alloy doping, and catalyst selection. Carbon-based spatial confinement is an effective approach to enhance the hydrogen storage and release performance of MgH_2. However, the underlying microscopic mechanisms and optimal synthesis strategies remain unclear, hindering the practical application and widespread adoption of this technology. In recent years, research has increasingly focused on exploring the potential of

---

* Corresponding author. Department of Power Engineering, School of Energy, Power and Mechanical Engineering, North China Electric Power University, Baoding, 071003, China.

E-mail address: yangwj@ncepu.edu.cn (W. Yang).

https://doi.org/10.1016/j.ijhydene.2025.06.177
Received 5 April 2025; Received in revised form 10 June 2025; Accepted 10 June 2025
0360-3199/

nanoscale spatial confinement. Wu et al. [14] studied MgH_2/CNT (5.9–15.7 nm) confined by carbon nanotubes, yielding hydrogen storage kinetic enhancement within a mere 1–20 wt% range. Also, as the initial pore size ratio of MgH_2/CNT increased from 0.41 to 0.61, the onset desorption temperature decreased from 369 °C to 337 °C. Jia et al. [15] found that in CMK-3 material, as the initial pore size ratio decreased from 0.5 to 0.18, the desorption temperature dropped from 152 °C to 102 °C. Notably, Peng et al. [16] synthesized carbon aerogel microspheres (CA) with highly folded surfaces and a mesh-like internal structure, using graphene sheets as carriers for MgH_2 particles, thus forming a MgH_2@CA core-shell structure. The hydrogen absorption and desorption enthalpies of MgH_2@CA were 63.34 kJ/mol and 69.57 kJ/mol, respectively, both lower than the standard 75 kJ/mol for pure MgH_2, indicating a reduction in thermodynamic stability. With regard to hydrogen storage performance, MgH_2@CA significantly lowered the onset desorption temperature to 105 °C and was capable of absorbing absorb 6.2 wt% H_2 within 5 min at 275 °C. Furthermore, Nayak et al. [17] modified MgH_2–Mg_2Ni nanocomposites with CNTs, achieving a hydrogen storage capacity of 5.78 wt% (99.88 % of the high reversible capacity from MgH_2 to BNCTs) with minimal degradation after 10 cycles [18]. However, challenges remain in developing and designing a new system. To diversify the specific systems of carbon materials in hydrogen storage applications, Simanullang et al. [19] investigated the spatial nanoconfinement effect of fullerenes (C_n) on MgH_2, finding it exhibited reversible hydrogen storage under mild conditions (10 bar and 150 °C) [20]. In the recent fervor of scientific exploration, Kassaoui [21] et al. delved into the dehydrogenation thermodynamics of Mg_nH_m nanoclusters of varying sizes (spanning from 0.5 to 2.8 nm), revealing that as the dimensions of the Mg_nH_m nanoclusters expand, their formation energy undergoes a significant enhancement, ascending from -65.12 kJ/mol for the 0.5 nm nanocluster to -51.37 kJ/mol for the 2.8 nm counterpart. Compared to bulk MgH_2, nanoclusters are less stable and more prone to hydrogen desorption. Concurrently, Razouk et al. [22] embarked on a theoretical investigation of the hydrogenation properties of two-dimensional MgH_2, determining its formation enthalpy to be -49.82 kJ/molH_2, a value notably inferior to the -63.018 kJ/molH_2 characteristic of bulk MgH_2. This finding underscores that the studied two-dimensional material, upon the introduction of Mg vacancies, not only attains a lower dehydrogenation temperature but also approaches the desirable ambient conditions.

These studies suggest that carbon material modification of MgH_2 could be a fundamental solution to the issues in magnesium-based solid-state hydrogen storage and transportation. However, they mainly focus on experimentally exploring the optimal carbon content and ball milling time, while the enhancement mechanism of MgH_2 dehydrogenation and the role of carbon carriers are not well understood. This lack of understanding likely stems from insufficient analysis of the dehydrogenation mechanism of MgH_2 under carbon carrier confinement.

Therefore, to explore the modification of magnesium-based hydrogen storage materials through the use of carbon carriers, we have undertaken pertinent research endeavors, incorporating both experimental data and theoretical simulations. Nonetheless, characterizing the surface of MgH_2 confined within fullerene poses several challenges, including material structural harmony, nanoscale intricacies, capturing swift dynamical shifts, and susceptibility to ambient conditions. Moreover, the distinctive spherical morphology of fullerene may give rise to intricate interfacial interactions with MgH_2, rendering the characterization of fullerene-confined MgH_2 and its hydrogen storage behavior a multifaceted, dynamic, and intricate endeavor. Furthermore, spatially confined nanomodels that entail substantial computational demands necessitate sophisticated algorithms and ample computational resources [23–25]. Thus, we leveraged Density Functional Theory (DFT) to describe the ground-state properties of the system through electron density rather than wavefunctions. However, given the computational intensity of this system, we integrated ORCA with the advantages of Density Functional Theory (DFT) to significantly reduce computational complexity, thereby overcoming a critical technological challenge in the hydrogen storage field.

In this work, we use fullerenes (C_n) as confinement matrices, integrating experimental and theoretical approaches to elucidate dehydrogenation mechanisms. By systematically varying C_n diameters and MgH_2 particle sizes, we establish the particle-to-pore ratio as a key determinant of hydrogen storage performance. Boron and phosphorus doping are introduced to optimize dehydrogenation kinetics. Using DFT in conjunction with ORCA, we analyze the electronic structure, H–Mg bond activation, and interfacial charge transfer within MgH_2-C_n systems. Crucially, we investigate the influence of particle size distribution and pressure on dehydrogenation onset temperature, aiming to refine thermodynamic and kinetic properties. Through comprehensive structural analysis and experimental validation, this work provides a robust theoretical framework for designing high-performance magnesium-based hydrogen storage materials with reduced dehydrogenation temperatures, accelerating the advancement of hydrogen energy technologies.

2. Method

In this study, the RIJCOX method [26] was employed to speed up the calculations overall. We utilized the ORCA 5.0.3 package, grounded in density functional theory (DFT) [27,28], to conduct the calculations, including structural optimization and frequency analysis, while fully accounting for zero-point energy. The VMD [29] was employed for visualization and result plotting. To ensure both conciseness and accuracy, the PBE0-D3 functional along with the def2-TZVP(-f) basis set (incorporating DFT-D3) was employed to perform structural optimization and frequency calculations [30,31]. For single-point energy computations, the B3LYP hybrid functional with the same basis set was applied, which is proven to match small organic systems.

The fullerene carbon sphere structures were constructed using Materials Studio and Avogadro software [32,33], with periodicity removed and hydrogenation applied to the shell.

The Molclus program [34], combined with MOPAC, utilized the PM6 functional to generate the ten lowest-energy configurations of $(MgH_2)_n$ ($n = 1 \sim 9$) nanoparticle clusters, from which the lowest energy structure was selected. This structure underwent geometric optimization and single-point energy calculations using the B3LYP hybrid functional and the def2-TZVP (-f) basis set (including DFT-D3). The following equation (1) can be used to calculate the formation energy of the MgH_2 clusters:

$$E_F = \mathrm{E}\left(\left(\mathrm{MgH_2}\right)_n\right) - n\mathrm{E}(\mathrm{Mg}) - n\mathrm{E}(\mathrm{H_2}) \tag{1}$$

where E_F is the formation energy [35] of the MgH_2 nanocluster, E($(MgH_2)_n$) is the total energy of the MgH_2 nanocluster, E(Mg) is the energy of a single Mg atom, and E(H_2) is the energy of H_2.

Our attention is centered on pivotal indicators of MgH_2 hydrogen sequestration and release kinetics, encompassing binding energy, H–Mg bond length, Mayer level, and initial dehydrogenation temperature. We scrutinize factors such as the particle size-to-diameter ratio and doping density to ascertain the optimal material parameters.

To further investigate the anti-agglomeration and nanoscale confinement effects of pristine/modified carbon spheres on MgH_2 nanoparticles, the binding energy E_B between the $(MgH2)_n$ cluster (structure A) and the pristine/modified carbon sphere (structure B) was calculated as follows:

$$E_B = \mathrm{E(AB)} - \mathrm{E(A)} - \mathrm{E(B)} + \mathrm{E}_{BSSE} \tag{2}$$

$$E_{BSSE} = (\mathrm{E(A)} - \mathrm{E}_{AB}(\mathrm{A})) + (\mathrm{E(B)} - \mathrm{E}_{AB}(B)) \tag{3}$$

$$E_B = \mathrm{E(AB)} - \mathrm{E}_{AB}(\mathrm{A}) - \mathrm{E}_{AB}(B) \tag{4}$$

where E(AB) is the total confinement energy of MgH_2 nanoparticles within the pristine/modified carbon spheres, E(A) is the energy of the

$(MgH_2)_n$ cluster nanoparticle, E(B) is the energy of the pristine/modified carbon sphere, and $E_{AB}(A)$ and $E_{AB}(B)$ are the energies of the $(MgH_2)_n$ cluster and the pristine/modified carbon sphere, respectively, corrected for basis set superposition error (BSSE).

To further demonstrate the influence of the particle-to-carbon sphere size ratio on the dehydrogenation performance of MgH_2 nanoparticles within carbon spheres, we focused on the H–Mg bond lengths, charge distribution, Mayer bond orders and ELF [36,37] maps, analyzed using the Multiwfn [38] program, developed by Lu Tian, based on wave function analysis.

According to theoretical analysis, the adsorption and desorption behavior of H_2 at a given temperature and pressure can be characterized by the relative energy E_r, defined as:

$$E_r = E(AB) - E(A) - nE(Mg) - n\left[E(H_2) + \mu_{H_2}(T,P)\right] \tag{5}$$

where $E(AB)$, $E(A)$, $E(Mg)$ and $E(H_2)$ represent the total energies of the carbon-confined MgH_2 system, the carbon-based carrier, Mg and the H_2 molecule, respectively. The term $\mu H_2(T,P)$ denotes the chemical potential of H_2 at a given temperature and pressure, which can be determined using the following equation:

$$\mu_{H_2}(T,P) = \Delta H - T\Delta S + k_B T \ln\frac{P}{P_0} \tag{6}$$

where p_0 refers to the standard atmospheric pressure (0.1 MPa), k_B is the Boltzmann constant [42], and ΔH and ΔS represent enthalpy and entropy changes, respectively. The value of $\Delta H - T\Delta S$ can be obtained from thermochemical tables [43]. The critical temperature (T_c) [22] is determined by numerically solving $E_r = 0$ in Equation (5), which marks the thermodynamic equilibrium between hydrogen adsorption and desorption. Here, H_2 integrates standard enthalpy (ΔH) and entropy (ΔS) values from Ref. [43].

3. Results and discussion

3.1. Model establishment

To investigate the interplay between particle size and fullerene C_n diameter, aiming to optimize the dehydrogenation performance of MgH_2 nanoparticle clusters confined in C_n , we constructed C_n with different diameters: C_{180} (1.2 nm, comprising 180 carbon atoms with 12 pentagons and 150 hexagons, Fig. S2) and C_{240} (1.34 nm, comprising 240 carbon atoms with 12 pentagons and 228 hexagons, Fig. S3). Additionally, as is shown in Fig. 1a and b, the optimal configurations of nanoparticle clusters (e.g. Mg_2H_4, Mg_4H_8, Mg_8H_{16}) were determined. Fig. 1a illustrates the $(MgH_2)_n$ (n = 3, 6, 9) cluster structures under varying diameters of C_n confinement. The C–C bond lengths of benzene rings in carbon nanotubes are depicted, where the edge length shared between hexagons and pentagons is approximately 1.45 Å, and the edge length between hexagons is about 1.4 Å. This curvature, induced by the fullerene sphere at the microscopic level, causes the pentagonal structures to be relatively bent, while the hexagonal structures remain relatively flat. Consequently, pentagonal bond lengths are more susceptible to strain, resulting in slightly shorter bond lengths compared to hexagonal ones. These results align with previous experimental and theoretical values, thereby validating the standardization of our graphene sphere model [39].

To obtain low-energy MgH_2 nanoparticles of varying sizes and structures, we systematically optimized the configurations of 200 $(MgH_2)_n$ (n = 1~9) clusters. Through trend analysis, we identified locally favorable energy configurations among these 200 possible structures, calculating their particle sizes and formation energies. The calculated particle sizes for the $(MgH_2)_n$ (n = 1~9) clusters are 0.343 nm, 0.439 nm, 0.513 nm, 0.594 nm, 0.630 nm, 0.641 nm, 0.675 nm, 0.716 nm, 0.847 nm, and 0.874 nm, respectively. As is shown in Fig. 1b, the formation energy (eV) of MgH_2 increases with n, indicating a tendency for MgH_2 to aggregate into larger clusters under standard conditions. The scatter plot, accompanied by three-dimensional molecular structures, further visualizes the geometric shapes and configurations of nanoparticles with different sizes.

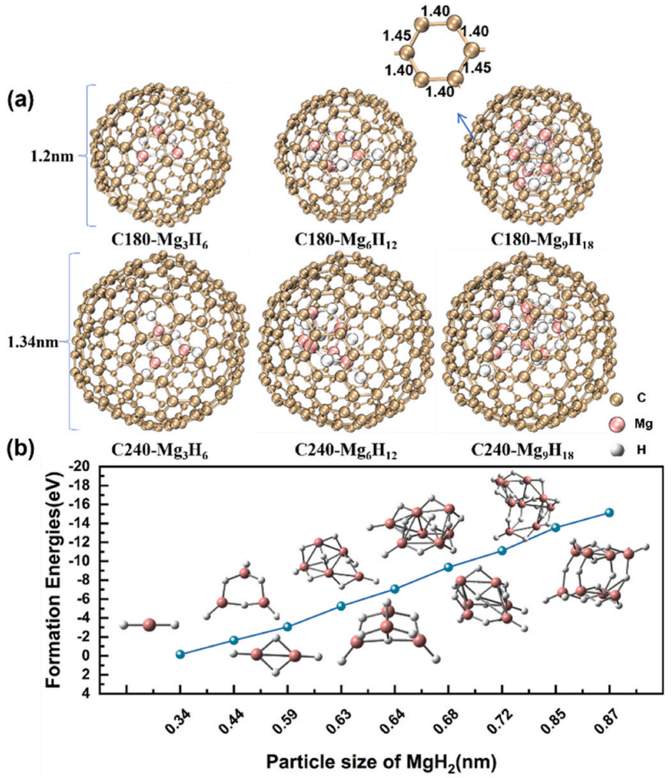

Fig. 1. (a) C_n structures with different diameters (1.2 nm and 1.34 nm), and the $(MgH_2)_n$ (n = 3, 6, 9) cluster structures under each diameter of C_n confinement; (b) Formation energy and structures of $(MgH_2)_n$ (n = 1~9) nanoparticles with varying sizes.

On the other hand, to further investigate and quantify the charge transfer process, we used the Multiwfn software [38] to generate 3D (Fig. 2a-e) and 2D charge density difference maps (Fig. 2f-j) for the optimal structure of 1.01 wt%B-doped 1.2 nm C_{180} confined $(MgH_2)_n$ clusters (n = 1, 3, 5, 7, 9), and subsequently calculated the CM5 charge transfer values. In these models, positive values (green) represent charge accumulation regions, and negative values (blue) represent charge depletion regions. Red arrows indicate the CM5 charge transfer values and the charge transfer paths. We observed significant charge accumulation near the interface between the $(MgH_2)_n$ clusters and the C_{180} walls. Additionally, the charge transfer process in the confined $(MgH_2)_n$ cluster structures was demonstrated, with electrons diffusing from C_n to the interior of the $(MgH_2)_n$ cluster. Based on the changes in electron density and distribution across the system, we found that as the particle-to-pore size ratio of MgH_2 and C_n increases, the CM5 charge density transfer also raises (Fig. 2k-o). The electron localization function (ELF) reveals the degree of electron localization within the molecule, reflecting the bonding characteristics of the structure. As n increases in the $(MgH_2)_n$ clusters, the number of high-electron localization regions (red areas) in the ELF map increases, and their total area grows, indicating a more dispersed electron distribution in the MgH_2 structure and a redistribution of covalent bonds, consistent with the trend of electron transfer from the center to the interface.

3.2. Structural stability

Owing to the prohibitive computational costs and extensive time required for AIMD simulations of such large systems using ORCA, the

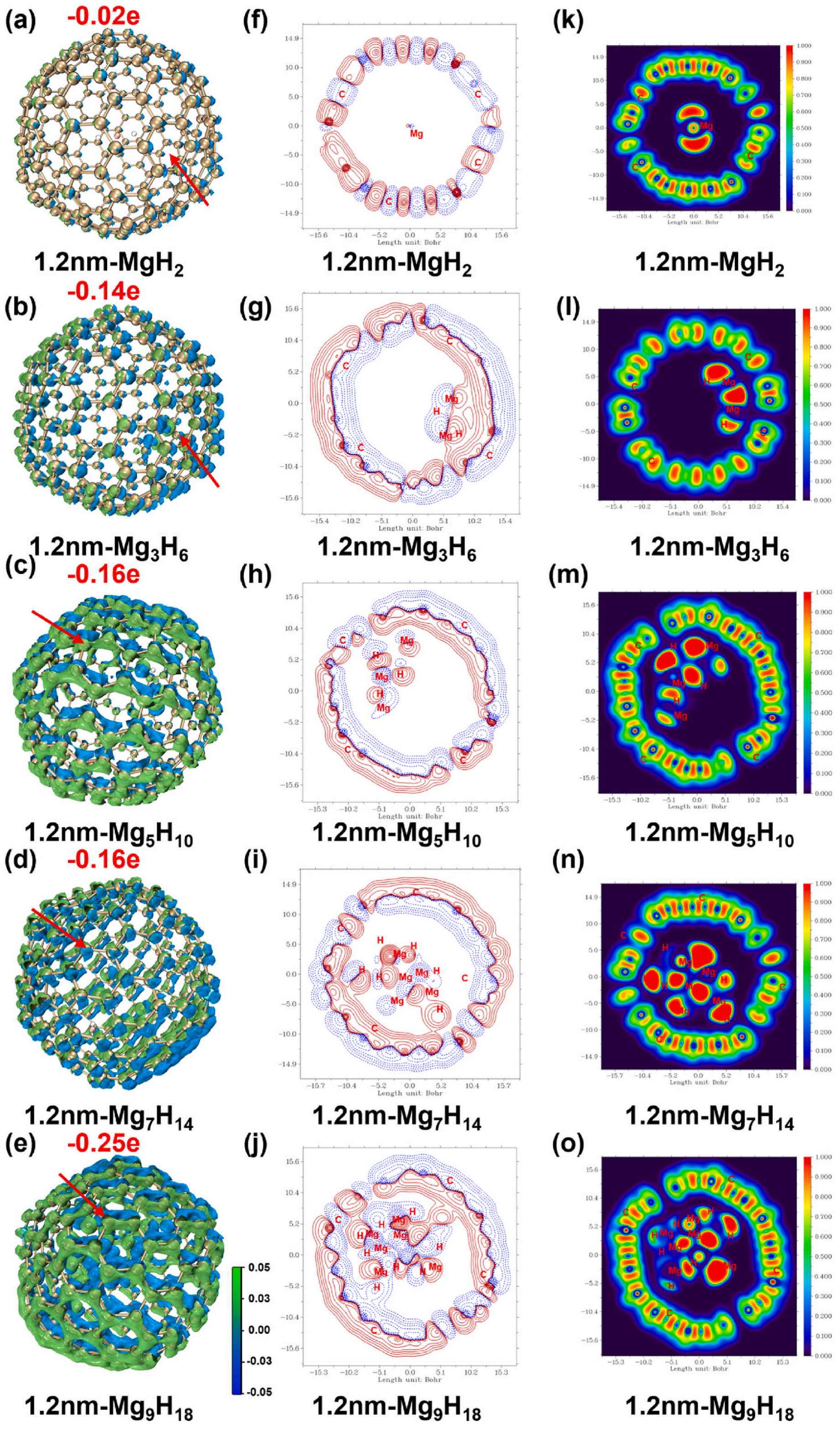

Fig. 2. 3D charge density difference maps (a–e), 2D charge density difference maps (f-j, cross-section fixed on planes based on B-34, C-91, and C-136), and ELF (Electron Localization Function) maps (k–o) of the optimal structure of 1.01 wt% B-doped 1.2 nm C_{180}.

feasibility is currently low. Using the structural optimization above, we calculated the binding energy of MgH_2 clusters confined in C_n and plotted the relationship between binding energy and the ratio of particle size to diameter in Fig. 3. As the ratio of MgH_2 particle size to C_n diameter increases, the binding energy of the C_n-confined MgH_2 structure becomes negative, with the absolute value of the negative binding energy increasing, indicating enhanced stability of the C_n confinement system. In the doping study, as is shown in Fig. 3a and b, the optimal binding energy ranges for the 0.75 wt% B-doped and 1.01 wt% B-doped fullerene particles are distinct. Specifically, when the particle size-to-diameter ratio is within 0.45–0.6, the CM5 charge transfer in the 0.75 wt% B-doped fullerene structure is higher than that in the 1.01 wt% B-

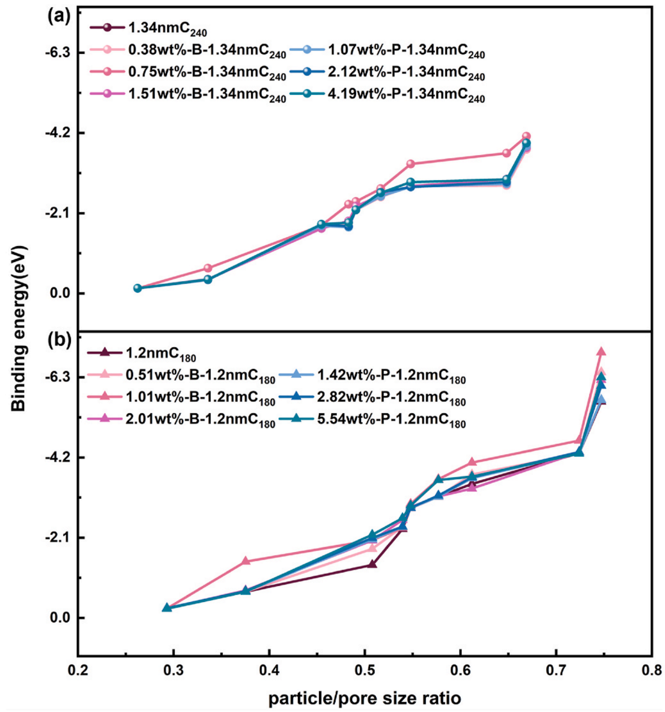

Fig. 3. Relationship between the ratio of MgH_2 nanoparticle size to C_n pore diameter and the average binding energy in MgH_2 nanoparticles.

doped fullerene structure. This higher charge transfer leads to stronger interactions and optimal binding energy in this range. Conversely, when the ratio is between 0.3-0.45 and 0.6–0.8, the CM5 charge transfer in the 1.01 wt% B-doped fullerene structure is higher, resulting in stronger interactions and optimal binding energy within these ranges. The interaction strength, influenced by the amount of charge transfer, in turn affects the binding energy and structural stability. These findings highlight the importance of tuning the boron doping concentration to optimize hydrogen storage properties. The optimal doping structures of confined $(MgH_2)_n$ ($n = 1\sim9$) at C_{180} and C_{240} are shown in Fig. S4–S5. To investigate the stability of the composite, we have analyzed the binding energy between $(MgH_2)_n$ clusters and Cn fullerene in the manuscript. Our calculations reveal a binding energy as high as -6 eV, coupled with significant charge transfer, indicating a very strong interaction. Recognizing the importance of validating stability and exploring adsorption dynamics through simulations, we plan to use periodic simulation software like VASP for more extensive AIMD simulations in future research.

Doping with B and P elements allows for precise modulation of the dehydrogenation dynamics of MgH_2 nanoparticles by adjusting their concentrations, making them more adaptable to different application requirements. Fig. S6–S8 succinctly illustrate the effects of boron(B) and phosphorus (P) doping on binding energy, H–Mg bond length, and Mayer bond order. We also compared the influence of doping on various C_n diameters and particle size-to-pore ratio values. For C_n with larger diameters and particle size-to-pore ratios, doping has a more pronounced effect on binding energy, yet no clear correlation is observed for bond length and Mayer bond order. Based on various B/P doping concentrations, we constructed schematic illustrations of C_{180} and C_{240} carbon-based carriers with different doping levels (Fig. S1).

From the three figures, Fig. S6 reveals that B doping typically leads to a significant reduction in the binding energy of MgH_2nanoparticles. This reduced binding energy implies that the MgH_2 structure is more likely to interact with the surrounding environment, thus promoting hydrogen release. However, the binding energy does not continuously decrease with increasing B concentration, but instead reaches a peak. As shown in the figure, the extremum occurs at approximately 0.75 wt% (C_{180}) and 1.01 wt% (C_{240}) in the experimental range. For P doping, although it may slightly increase the stability of the H–Mg bond in some cases, at larger particle size-to-pore ratios, P doping can also reduce the binding energy, particularly near the fullerene wall, further enhancing the dehydrogenation kinetics. Fig. S7 indicates that, for certain particle size-to-pore ratios, the H–Mg bond length increases with higher B doping concentrations. However, for C_{180} in the 0.51–0.61 particle size-to-pore ratio range and C_{240} in the 0.52–0.67 range, the bond length initially shortens and then increases as B doping concentration rises. The data suggest that P doping affects H–Mg bond length differently under varying conditions and can be tailored based on specific needs. Fig. S8 shows that B doping significantly lowers the average Mayer bond order of the H–Mg bond, indicating that the bond becomes more ionic and prone to breaking, which is advantageous for improving MgH_2 dehydrogenation efficiency. P doping, however, exhibits a more complex influence on dehydrogenation kinetics. The variation in doping concentration leads to different adjustments in H–Mg bond stability. Overall, P doping may enhance dehydrogenation performance under certain conditions but requires optimization based on concentration. Therefore, to investigate the stability of the composite, we have analyzed the binding energy between $(MgH_2)_n$ clusters and Cn fullerene in the manuscript. Our calculations reveal a binding energy as high as -6 eV, coupled with significant charge transfer, indicating a very strong interaction.

3.3. H–Mg bonding properties

Based on the optimized structures mentioned above, the average H–Mg bond length in all structures was calculated and plotted against the particle size to C_n diameter ratio as is shown in the line graph in Fig. 4. Each curve represents the trend for different doping levels, with the average H–Mg bond length for each data set indicated by values such as Avg: 1.87 Å and Avg: 1.92 Å. In the C_n -nanoconfined Mg_9H_{18} structure (the series with the largest particle size to pore size ratio), the average H–Mg bond length is approximately 1.92 Å, making it the structure with the longest bond length. The shortest H–Mg bond length is 1.73 Å in the MgH_2 structure, which is in excellent agreement with experimentally determined H–Mg bond lengths, thus validating the accuracy of our calculation range [40,41].

Overall, in Fig. 4a and b, all curves depict an increasing trend in the average H–Mg bond length as the particle size to pore size ratio increases. Both plots display a similar growth trend, with a rapid increase in bond length in the small particle size to pore size ratio range (approximately 0.3–0.37); a plateau phase in the intermediate range ($0.35 <$ particle size to pore size ratio <0.55); and a new growth trend in the higher ratio range (>0.55). For different C_n diameters, the H–Mg bond length in the C_{180} (1.2 nm) confinement is generally longer than in the C_{240} (1.34 nm) confinement, with a noticeable difference in the high particle size to pore size ratio region. In the C_{180} (1.2 nm) structure, certain doped states (e.g., 2.01 wt% B and 5.54 wt% P) show more significant increases in H–Mg bond length (up to 1.92 Å), indicating that doping elements (B, P) have an additional impact on H–Mg bond length, enhancing the nanoconfinement effect and further increasing the bond length in certain regions.

In addition, we calculated the Mayer bond order of all H–Mg bonds in the C_n nanoconfined MgH_2 nanoparticle structures. The average Mayer bond order of the H–Mg bonds in both figures shows a similar trend. Initially, for smaller particle size to pore size ratios (approximately 0.2–0.3), the Mayer bond order is relatively high (close to 0.85). For H–Mg bonds in the 1.34 nm pore size structure, the Mayer bond order exhibits a significant decrease within the 0.25–0.35 and 0.46–0.55 ratio ranges (Fig. 5a). In the 1.2 nm pore size structure, the Mayer bond order significantly decreases within the 0.3–0.8 and 0.5–0.62 ratio ranges (Fig. 5b). In the larger particle size to pore size ratio region (larger than 0.6), the Mayer bond order stabilizes or changes minimally. Comparing

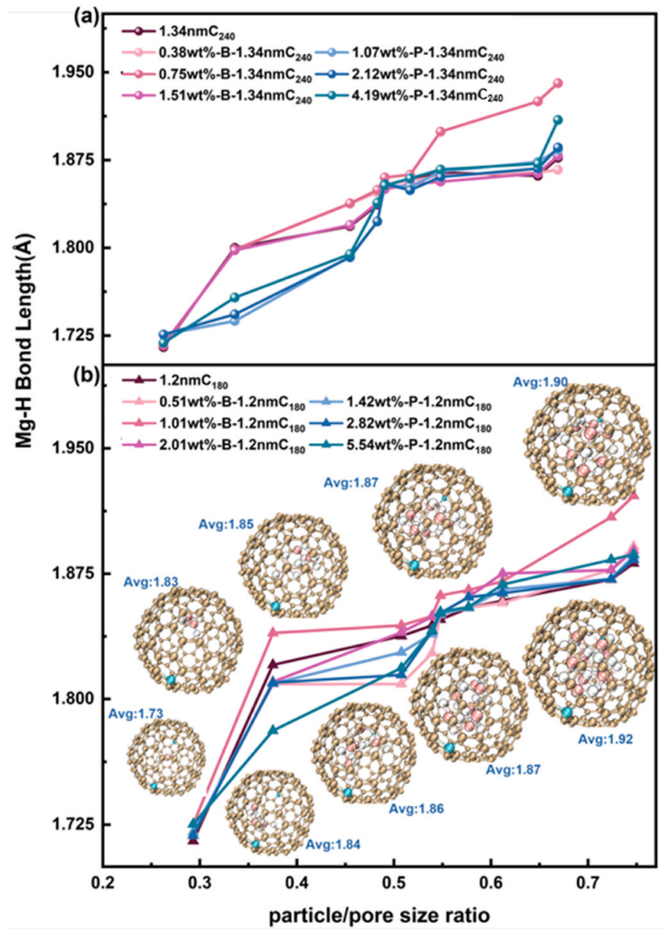

Fig. 4. Relationship between the ratio of MgH_2 nanoparticle size to C_n pore diameter and the average H–Mg bond length in MgH_2 nanoparticles.

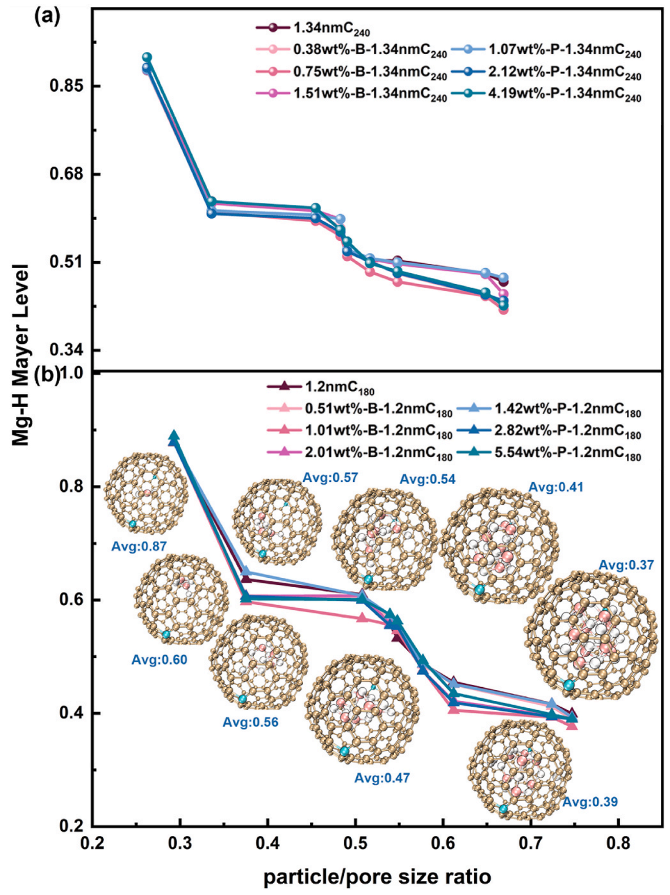

Fig. 5. Relationship between the ratio of MgH_2 nanoparticle size to C_n pore diameter and the average Mayer level of all H–Mg bonds in MgH2 nanoparticles.

the two C_n diameters, particularly for particle size to pore size ratios above 0.5, the Mayer bond order in the 1.2 nm C_{180} structure is significantly lower than in the 1.34 nm C_{240} structure (Fig. 5a). Moreover, we considered the impact of element doping on the Mayer bond order. As is shown in the figure, doping with B elements (such as 0.51 wt% B or 2.01 wt% B) and P elements (such as 2.82 wt% P) results in a slight decrease in Mayer bond order. However, doping with 2.82 wt% P leads to an increase in the Mayer bond order. Thus, selecting the appropriate doping concentration is beneficial for enhancing the dehydrogenation kinetics of MgH_2 nanoparticle structures confined in C_n.

We also present the overall optimal distribution model of the H–Mg Mayer levels in the $(MgH_2)_n$ ($n = 1\sim9$) series structure doped with 0.51 wt% B in C_n with a 1.2 nm diameter. From all figures and data, it is evident that in the fullerene structure, the Mayer bond order of H–Mg bonds near the pore walls is lower compared to those farther from the walls. This suggests that these bonds exhibit weaker covalency and are more prone to rupture. In the absence of wall interference, the Mayer bond order of these bonds is generally greater than 0.8. In addition, the H–Mg bonds located on the outer layer of the cluster tend to have lower Mayer bond orders compared to those on the inner layer. As the particle size to pore size ratio increases, the difference in Mayer bond order between the outer and inner layers becomes more pronounced, indicating that with the introduction of spatial confinement, the aggregate bond strength becomes more heterogeneous. As the particle size to pore size ratio increases from 0.28 to 0.75, the Mayer bond order of H–Mg bonds gradually decreases, indicating a more significant weakening effect on the H–Mg bonds. In conclusion, the nanoconfinement of C_n effectively promotes the dehydrogenation kinetics of MgH_2 clusters within the particle size to pore size ratio range of 0.28–0.75.

3.4. *Onset dehydrogenation temperature*

Fig. 6 and Fig. S9 illustrate the variation of relative energy (E_r) as a function of temperature for different $(MgH_2)_n$ ($n = 1\sim9$) clusters supported on 1.01 wt% B-doped C_{180} and 0.75 wt% B-doped C_{240} under varying pressures. The critical temperature (T_c), defined by the intersection of E_r with zero (Fig. 6), demarcates the onset of spontaneous dehydrogenation. For 1.01 wt% B-doped C_{180}, T_c drops to 378–447 K at 0.1 MPa, a 150K reduction versus unconfined MgH_2. This shift arises from weakened H–Mg bonds under nanoconfinement, as quantified in Section 3.3.

Notably, adjusting the particle size-to-pore diameter ratio can significantly reduce the dehydrogenation temperature, which is of great significance for the design of practical hydrogen storage systems. For example, in vehicular hydrogen storage systems that require rapid hydrogen release at moderate temperatures (50–100 °C), our prediction shows that the dehydrogenation temperature of 1.01 wt% B-doped C_{180} at a ratio of 0.9 can be as low as 69.26 °C, demonstrating the feasibility of using fullerene-confined MgH_2 without external heating.

According to the definition of relative energy (E_r), a negative E_r value indicates that the adsorption state of H_2 is energetically more favorable than the desorption state, implying enhanced H_2 adsorption. Comparative analysis reveals that, under different pressure conditions, E_r increases with rising pressure across all $(MgH_2)_n$ clusters, transitioning from an initial negative value to a positive one, signifying a shift in the composite material from hindered desorption to facilitated desorption. A cross-pressure comparison indicates that a decrease in pressure leads

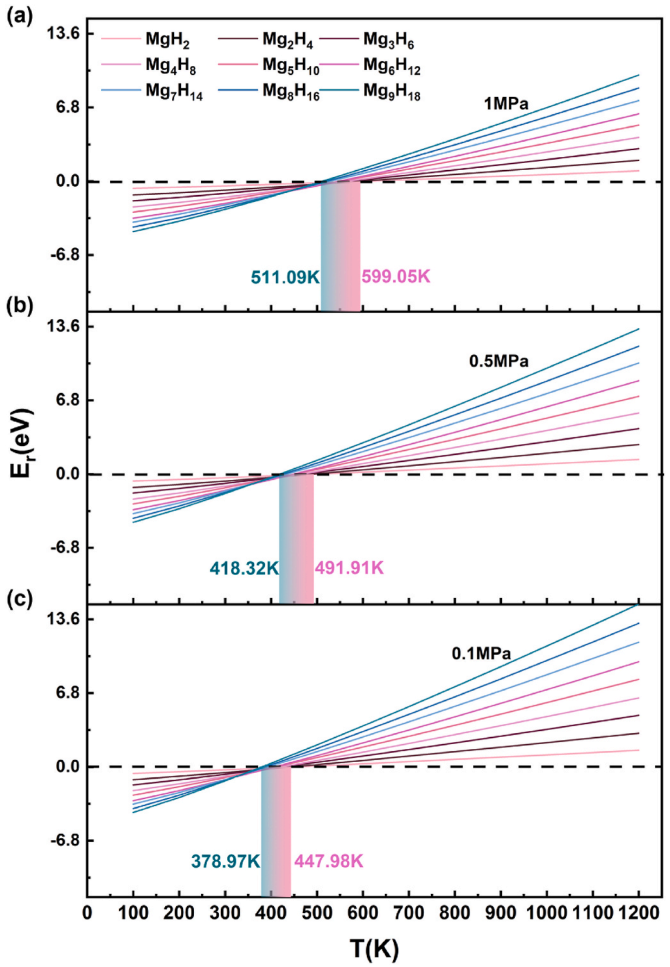

Fig. 6. Temperature-dependent variation of relative energy for $(MgH_2)_n$ (n = 1–9) clusters of varying sizes confined within 1.01 wt% B-doped C_{180} under different pressures: (a) 1 MPa, (b) 0.5 MPa, and (c) standard atmospheric pressure (P = 0.1 MPa).

to a reduction in the onset dehydrogenation temperature. In Fig. 6c, under standard atmospheric pressure, the critical temperature (T_c) drops to approximately 378–447 K. At this temperature, the adsorption-desorption energy difference is minimal, resulting in improved kinetic performance and stability. Notably, we investigated the temperature-dependent variation of relative energy for $(MgH_2)_n$ clusters of different sizes in 1.01 % B-doped C_{180} under 0.1 MPa, as shown in Fig. S11. The image indicates that the hydrogen absorption temperature of H_2 molecules by hydrogen free Mg nanoclusters in the C_{180} domain doped with 1.01 wt% B is 394.95K. Furthermore, an examination of different curves within the same figure reveals that as cluster size increases, the variation in E_r becomes more pronounced, indicating more intense H_2 adsorption-desorption interactions, which further hinder the improvement of desorption kinetics.

Fig. 7 and Fig. S10 investigate the pressure dependence of relative energy (E_r) for different $(MgH_2)_n$ (n = 1~9) clusters confined within 1.01 wt% B-doped C_{180} and 0.75 wt% B-doped C_{240} at varying temperatures. As pressure increases, E_r decreases until it becomes negative, indicating the cessation of dehydrogenation. However, when E_r approaches zero, a certain pressure range allows for relatively stable dehydrogenation. Studies reveal that at 500 K, stable dehydrogenation occurs within 1~11 bar, while at 700 K, it extends to 1–10 bar. Comparing clusters of different sizes, smaller n values exhibit smaller E_r variations and a broader range for optimal stable dehydrogenation.

3.5. Mechanism analysis

The use of fullerene nanoconfined MgH_2 nanoparticles to improve dehydrogenation kinetics is mainly attributed to mechanisms involving electronic structure modulation, H–Mg bond polarization, interface effects, and defect introduction. In the C_n fullerene structure, all carbon atoms are SP^2 hybridized, forming a combination of five-membered and six-membered rings. This topology results in π-electrons being distributed across the spherical surface, creating a broad π-conjugated system. This conjugated property gives fullerene unique interface charge effects, enabling electronic interactions with MgH_2 nanoparticles. Under C_n confinement, the electron density around Mg changes, weakening the Coulomb attraction between H–Mg. Additionally, charge accumulation at the Mg/C_n interface creates a charge separation region, facilitating hydrogen dissociation.

Moreover, based on the theoretical findings, we conducted a correlation analysis between the Mayer bond order of H–Mg bonds and the CM5 charge transfer. We first investigated the nanoconfinement of pristine C_{180} and C_{240} structures, where each data point corresponds to a specific CM5 charge transfer value and its associated H–Mg Mayer bond index. As CM5 charge transfer increases (shifting positively), the H–Mg Mayer bond index rises accordingly. A linear fit of the data yielded the equation $y = 1.65x + 0.83$ with an R^2 value of 0.93 (Fig. 8a), indicating a strong linear correlation. This further substantiates the influence of electronic structure on dehydrogenation performance. Afterwards, we selected C_n structures with different pore sizes and varying concentrations of B and P atoms, recording the H–Mg bond Mayer order and CM5 charge transfer values for each group. After fitting the data points, we obtained the fitting line: $y = 1.67x + 0.81$, with an R^2 value of 0.84 (Fig. 8b), indicating a high degree of correlation. This fitting process shows a clear linear relationship between the charge transfer and Mayer bond order in the C_n confined structures, where an increase in CM5 charge transfer leads to a higher Mayer bond order for the H–Mg bond. Similar trends were observed when compared to the relationships between particle size ratio, binding energy, H–Mg bond length, and Mayer

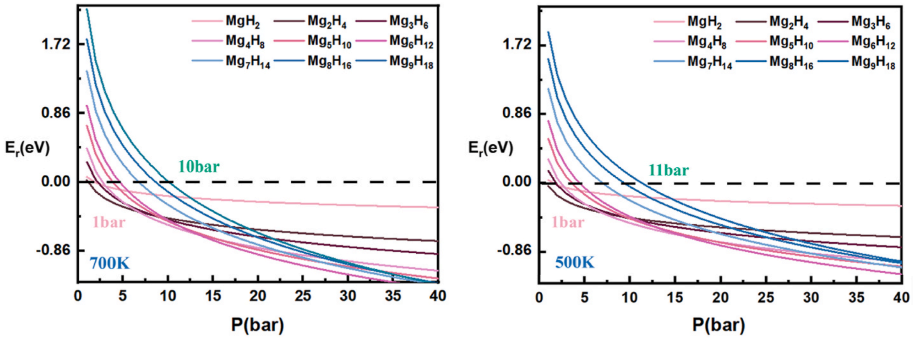

Fig. 7. Pressure-dependent variation of relative energy for $(MgH_2)_n$ (n = 1~9) clusters of varying sizes confined within 1.01 wt% B-doped C_{180}: (a) 700 K, (b) 500 K.

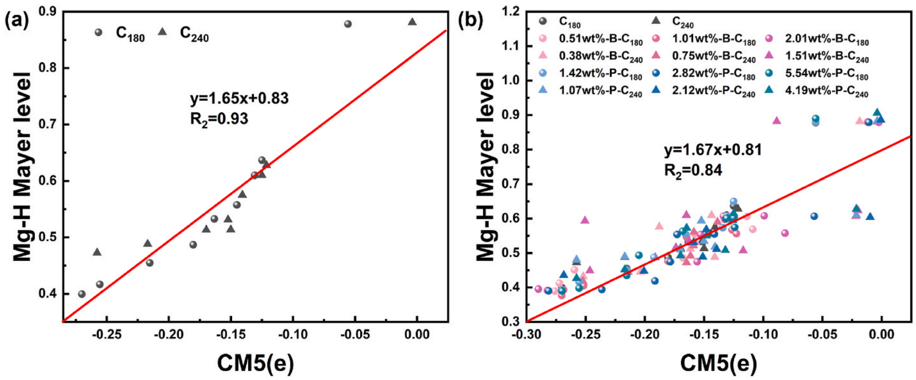

Fig. 8. Comparison of two optimal series in fullerenes and three in carbon nanotubes: (a) Correlation between CM5 charge transfer and H–Mg bond Mayer index under the nanoconfinement of pristine C_{180} and C_{240} structures; (b) Correlation between CM5 charge transfer and H–Mg bond Mayer index under the nanoconfinement of different diameters and B doping concentrations.

bond order, further validating the correctness of our conclusions.

3.6. Materials comparison

Finally, we summarize the impact of varying MgH_2 particle size-to-diameter (or pore size) ratio within different carbon-based supports (fullerene C_ns, carbon aerogels CAs [44,45], Carbon-based Template CT [44], CMK-3 [15], carbon nanotubes CNTs [46,47], and Graphitized Carbon GC [48]) on the onset dehydrogenation temperature of MgH_2 nanoparticles according to Table 1, as observed in previous studies.

Specifically, we compared the kinetic characteristics of various C_n materials with the promising carbon-based supports CNT and CMK-3 from multiple perspectives. C_n materials show significant differences from CNTs in terms of H–Mg bond length, Mayer bond order, and onset dehydrogenation temperature. Our calculations indicate that the C_n materials generally exhibit longer average H–Mg bond lengths (Fig. 9a), lower Mayer bond orders for the H–Mg bond (Fig. 9b), and can achieve lower onset dehydrogenation temperatures, as seen in the experimental data for 1.01 wt% B-doped 1.2 nm C_{180} (Fig. 10a). Compared to CMK-3, curve fitting predicts that the onset dehydrogenation temperature of 1.01 wt% boron-doped 1.2 nm C_{180} can drop to 69.26 °C at a particle size-to-pore size ratio of 0.9, a decrease of 33°C—marking a breakthrough in optimizing dehydrogenation temperature. At the same ratio, C_n materials exhibit notably lower dehydrogenation temperatures, covering the applicability of the CMK-3 system. This suggests that C_n materials, when appropriately doped and nano-confined, can undergo stable dehydrogenation over a wide temperature range and are suitable for more stringent and lower temperature conditions, making them a promising kind of confined materials.

3.7. Linear relationship between onset dehydrogenation temperature and nano-confined systems

The relationship between the onset dehydrogenation temperature and the particle-to-pore size ratio across various carbon-based supports is illustrated in Fig. 10a. The solid lines represent the experimental data obtained in this study, while the dashed lines correspond to theoretical predictions. Overall, as the ratio of the particle size of MgH_2 nanoparticles to the diameter of C_n increases, the Mayer bond order decreases, enhancing the weakening effect on the H–Mg bond, thereby lowering the dehydrogenation temperature of MgH_2. This indicates that increasing the ratio of particle size to diameter can improve the dehydrogenation kinetics of MgH_2 nanoparticles. The universal nanoconfinement mechanism inherent to various nanostructures ensures that interfacial charge redistribution on different substrates consistently weakens the H–Mg bond by a similar order of magnitude, yielding linear relationships with comparable slope values. Numerically, the slopes for these nanomaterials are found to be closely clustered. This fundamental consistency validates the scientific rationale for employing identical slope fitting across diverse nano-structural configurations. Notably, when performing linear fitting, the comparison using the same slope is more evident. All data points were fitted with a uniform slope of -184.39, exhibiting a highly consistent trend ($R^2 > 0.8$). This linear relationship provides a robust foundation for constructing predictive models of dehydrogenation temperatures, offering valuable theoretical guidance for the rational design of advanced hydrogen storage materials. It can be observed that the data for 1.01 wt% boron-doped 1.2 nm C_{180} lies above all other curves, exhibiting superior performance at any particle size ratio.

Fig. 10b shows the relationship between activation energy (E(A)) and the *b* values from the linear fitting, with *b* representing the intercept of the linear fitting equation in Fig. 10a. A linear fit for multiple data sets from different materials yields the equation: $y = -0.56x + 118.98$, $R^2 = 0.89$. This strong correlation ($R^2 = 0.89$) indicates a positive relationship between the absolute value of the E(A) and the b value, where lower b values correspond to reduced dehydrogenation activation energy. Referring back to Fig. 10a, this confirms the superior dehydrogenation performance of the C_n system. While the current study yields significant insights, the investigation of energy barriers and reaction heat in hydrogenation/dehydrogenation processes, which is computationally arduous, is left for future research endeavors.

Table 1
Comparison of particle size/pore size, and onset temperature for different carbon-based supports.

Material	Particle size/pore size	Onset temperature (°C)	References
CAs	0.52–0.8	210~265	[44,45]
CT	0.85	117	[44]
CMK-3	0.41–0.89	102~250	[15]
CNTs	0.41–0.61	337~367	[46,47]
GC	0.75	280	[48]
CNTs (calculate)	0.29–0.77	111~206	[23]
C_n(calculate)	**0.26~0.73**	**106~258**	**In this work**

4. Conclusions

To investigate the size-matching influence of fullerene configurations on encapsulated MgH_2 nanoparticles, this research primarily employs density functional theory (DFT) computations to establish two C_n structures with differing diameters: C_{180} with a diameter of 1.2 nm and C_{240} with a diameter of 1.34 nm, alongside nine $(MgH_2)_n$ ($n = 1$~9) clusters, based on optimal configurations derived from experimental literature. The computational results reveal that as the particle size-to-

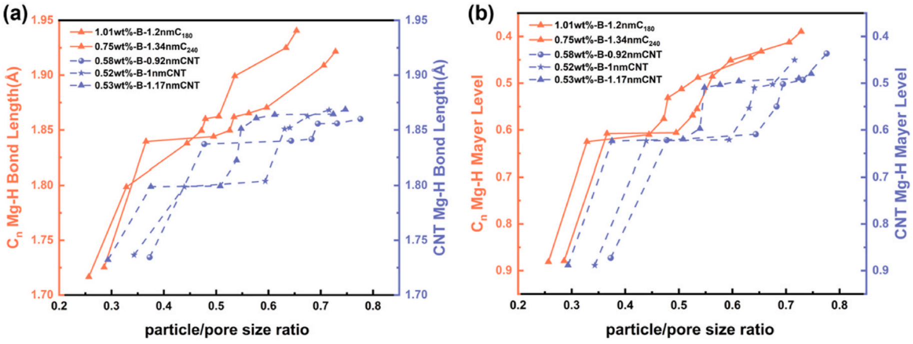

Fig. 9. Comparison of two optimal series in fullerenes and three in carbon nanotubes: (a) H–Mg bond length; (b) H–Mg bond Mayer index.

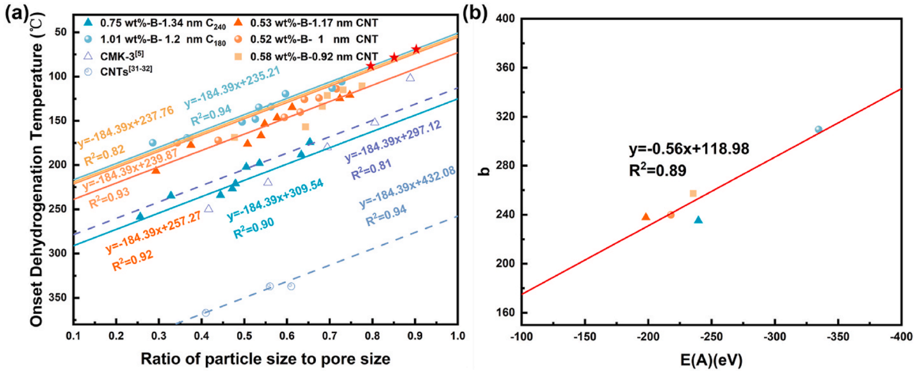

Fig. 10. (a) Relationship between particle-to-pore size ratio and onset dehydrogenation temperature in MgH_2 confined by all carbon-based supports; (b) Correlation between activation energy and linear fitting parameter b in different nanoconfined MgH_2 systems.

diameter ratio escalates within the range of 0.2–0.8, the mean H–Mg bond length augments, whereas the binding energy and Mayer bond index of H–Mg diminish.

Comparative analyses with alternative carbon-based materials, including carbon nanotubes (CNTs), corroborate that fullerene encapsulation offers distinctive benefits in optimizing hydrogen sequestration properties. By fine-tuning the particle size-to-pore diameter ratio and incorporating suitable doping, we significantly enhanced the hydrogen storage capacity and cycling stability of MgH_2. The strong linear relationship between CM5 charge transfer and the Mayer level of the H–Mg bond confirms the mechanism of enhanced dehydrogenation efficiency via fullerene nanoconfinement. Linear regression analysis shows that the onset dehydrogenation temperature of 1.01 % B-doped 1.2 nm C180 can be reduced to 69.26 °C at a particle size-to-pore diameter ratio of 0.9, 33 °C lower than the CMK-3 system, indicating the potential for ultra-low temperature dehydrogenation.

While the current study yields significant insights, the investigation of energy barriers and reaction heat in hydrogenation/dehydrogenation processes, which is computationally arduous, is left for future research endeavors. The study on the dehydrogenation performance of carbon-based confined MgH_2 provides important guidance for the design of practical hydrogen storage systems. Future research can prioritize the dehydrogenation performance of the predictive model proposed in this article to promote its practical application.

CRediT authorship contribution statement

Junyi Wo: Validation, Software, Investigation, Funding acquisition, Data curation, Conceptualization. **Weijie Yang:** Validation, Supervision, Methodology.

Declaration of interests

Data are available upon request from the authors.

Acknowledgments

This work was funded by the Natural Science Foundation of Hebei (E2023502006).

Appendix A. Supplementary data

Supplementary data to this article can be found online at https://doi.org/10.1016/j.ijhydene.2025.06.177.

References

[1] Allendorf MD, Stavila V, Snider JL, et al. Challenges to developing materials for the transport and storage of hydrogen. Nat Chem 2022;14(11):1214–23.
[2] Xu W, Tao Z, Chen J. Progress of research on hydrogen storage. Prog Chem 2006;18(2–3):200–10.
[3] Yanran W, Xiaowei C, Hongyu Z, Guanglin X, Dalin S, Xuebin Y. Heterostructures built in metal hydrides for advanced hydrogen storage reversibility. Adv Mater 2020;32:2002647.
[4] Xiaoyue Z, Yahui S, Shunlong J, Jikai Y, Xuechun H, Wei C, Long Y, Guanglin X, Fang F, Dalin S, Xuebin Y. Solar-Driven reversible hydrogen storage. Adv Mater 2023;35:2206946.
[5] Pang Y, Liu Y, Gao M, et al. A mechanical-force-driven physical vapour deposition approach to fabricating complex hydride nanostructures. Nat Commun 2014;5(1):3519.
[6] Zhang X, Ju S, Li C, et al. Atomic reconstruction for realizing stable solar-driven reversible hydrogen storage of magnesium hydride. Nat Commun 2024;15(1):2815.
[7] Zhang X, Liu Y, Ren Z, et al. Realizing 6.7 wt% reversible storage of hydrogen at ambient temperature with non-confined ultrafine magnesium hydrides. Energy Environ Sci 2021;14(4):2302–13.
[8] Li C, Yang W, Liu H, et al. Picturing the gap between the performance and US-DOE's hydrogen storage target: a data-driven model for MgH_2 dehydrogenation. Angew Chem 2024;136(28):e202320151.

[9] Dong S, Li C, Wang J, et al. The "burst effect" of hydrogen desorption in MgH 2 dehydrogenation. J Mater Chem A 2022;10(42):22363–72.
[10] Yang W, Ge H, Yao T, et al. Promotion mechanisms of LiBH$_4$ dehydrogenation dominated by charge redistribution. J Mater Chem A 2025;13(2):1014–22.
[11] Fu W, Yu K, Song H, et al. Design strategy of polyamine for CO$_2$ absorption guided by a novel descriptor of hydrogen bond strength. Fuel 2024;359:130393.
[12] Wu X, Xue H, Peng Y, et al. Research progress of Mg and Mg-based alloy hydrogen storage materials. Rare Met Mater Eng 2022;51(8):727–34.
[13] Kim KC, Dai B, Johnson JK, et al. Assessing nanoparticle size effects on metal hydride thermodynamics using the Wulff construction. Nanotechnology 2009;20 (20).
[14] Wu CZ, Wang P, Yao X, et al. Hydrogen storage properties of MgH2/SWNT composite prepared by ball milling. J Alloys Compd 2006;420(1–2):278–82.
[15] Jia Y, Sun C, Cheng L, et al. Destabilization of Mg-H bonding through nano-interfacial confinement by unsaturated carbon for hydrogen desorption from MgH$_2$. Phys Chem Chem Phys 2013;15(16):5814–20.
[16] Peng D, Ding Z, Zhang L, et al. Remarkable hydrogen storage properties and mechanisms of the shell-core MgH$_2$@carbon aerogel microspheres. Int J Hydrogen Energy 2018;43(7):3731–40.
[17] Zhang J, Xia G, Guo Z, et al. Synergetic effects toward catalysis and confinement of magnesium hydride on modified graphene: a first-principles study. J Phys Chem C 2017;121(34):18401–11.
[18] Liu M, Zhao S, Xiao X, et al. Novel 1D carbon nanotubes uniformly wrapped nanoscale MgH$_2$ for efficient hydrogen storage cycling performances with extreme high gravimetric and volumetric capacities. Nano Energy 2019;61:540–9.
[19] Simanullang M, Prost L. Nanomaterials for on-board solid-state hydrogen storage applications. Int J Hydrogen Energy 2022;47(69):29808–46.
[20] Ward PA, Teprovich JA, Peters B, et al. Reversible hydrogen storage in a LiBH$_4$-C$_{60}$ nanocomposite. J Phys Chem C 2013;117(44):22569–75.
[21] El Kassaoui M, Labrousse J, Loulidi M, et al. Ni/V-Mg $_n$ H $_m$ nanoclusters: recent advances toward improving the dehydrogenation thermodynamics for efficient hydrogen storage. Int J Hydrogen Energy 2024;89:272–8.
[22] Razouk A, Kassaoui MEL, Boubkri M, et al. Enhanced hydrogenation properties of two-dimensional MgH$_2$ by do**, vacancy-like defects and strain engineering: a theoretical study. Int J Hydrogen Energy 2024;92:1078–90.
[23] Fang L, Liu CK, Feng Y, et al. Size-dependent nanoconfinement effects in magnesium hydride. Int J Hydrogen Energy 2024;96:783–93.
[24] Dong S, Li C, Lv E, et al. MgH$_2$/single-atom heterojunctions: effective hydrogen storage materials with facile dehydrogenation. J Mater Chem A 2022;10(37): 19839–51.
[25] Dong S, Liu H, Liu X, et al. Facile dehydrogenation of MgH2 enabled by γ-graphyne based single-atom catalyst. J Energy Storage 2023;74:109484.
[26] Neese F, Wennmohs F, Hansen A, et al. Efficient, approximate and parallel Hartree-Fock and hybrid DFT calculations. A 'chain-of-spheres' algorithm for the Hartree-Fock exchange. Chem Phys 2009;356(1–3):98–109.
[27] Neese F. The ORCA program system. Wiley Interdiscip Rev-Comput Mol Sci 2012;2 (1):73–8.
[28] Neese F, Wennmohs F, Becker U, et al. The ORCA quantum chemistry program package. J Chem Phys 2020;152(22).
[29] Humphrey W, Dalke A, Schulten K. VMD: visual molecular dynamics. J Mol Graph 1996;14:33–8.
[30] Grimme S, Antony J, Ehrlich S, et al. A consistent and accurate ab initio parametrization of density functional dispersion correction (DFT-D) for the 94 elements H-Pu. J Chem Phys 2010;132(15).
[31] Weigend F, Ahlrichs R. Balanced basis sets of split valence, triple zeta valence and quadruple zeta valence quality for H to Rn: design and assessment of accuracy. Phys Chem Chem Phys 2005;7(18):3297–305.
[32] Hanwell MD, Curtis DE, Lonie DC, et al. Avogadro: an advanced semantic chemical editor, visualization, and analysis platform. J Cheminf 2012;4(17).
[33] Meunier M, Robertson S, Materials Studio 20th anniversary. Mol Simul 2021;47(7): 537–9.
[34] Lu T. Beijing kein research center for natural science. 2021. Beijing, China.
[35] Yang W, Xu S, Ma K, et al. Geometric structures, electronic characteristics, stabilities, catalytic activities, and descriptors of graphene-based single-atom catalysts. Nano Materials Science 2020;2:120–31.
[36] Fuster F, Grabowski SJ. Intramolecular hydrogen bonds: the QTAIM and ELF characteristics. J Phys Chem A 2011;115(35):10078–86.
[37] Rizhikov MR, Kozlovat SG, Konchenko SN. Electron structure of iron chalcogenide clusters {Fe3Q} from AIM and ELF data: effect of hydrogen atoms on interatomic interactions. J Phys Chem A 2009;113(2):474–9.
[38] Lu T, Chen FW. Multiwfn: a multifunctional wavefunction analyzer. J Comput Chem 2012;33(5):580–92.
[39] Friedrich M, Piovano P, Stefanelli U. The geometry of C60: a rigorous approach via molecular mechanics. SIAM J Appl Math 2016;76(5):2009–29.
[40] Intemann J, Spielmann J, Sirsch P, et al. Well-defined molecular magnesium hydride clusters: relationship between size and hydrogen-elimination temperature. Chem–Eur J 2013;19(26):8478–89.
[41] Peng B, Li L, Ji W, et al. A quantum chemical study on magnesium (Mg)/ magnesium–hydrogen (Mg–H) nanowires. J Alloys Compd 2009;484(1–2):308–13.
[42] Wang J, Du Y, Sun L. Ca-decorated novel boron sheet: a potential hydrogen storage medium. Int J Hydrogen Energy 2016;41(10):5276–83.
[43] Ma L, Wang L, Sun Y, et al. First-principles study of hydrogen storage on Ca-decorated defective boron nitride nanosheets. Phys E Low-dimens Syst Nanostruct 2021;128:114588.
[44] Peng JL, He YL, Zhou CY, et al. The carbon nanotubes-based materials and their applications for organic pollutant removal: a critical review. Chin Chem Lett 2021; 32(5):1626–36.
[45] Punetha VD, Rana S, Yoo HJ, et al. Functionalization of carbon nanomaterials for advanced polymer nanocomposites: a comparison study between CNT and graphene. Prog Polym Sci 2017;67:1–47.
[46] Hirshfeld FL. Bonded-atom fragments for describing molecular charge densities. Theor Chim Acta 1977;44:129–38.
[47] Iijima S. Helical microtubules of graphitic carbon. Nature 1991;354(6348):56–8.
[48] Zhang J, Xia GL, Guo ZP, et al. Synergetic effects toward catalysis and confinement of magnesium hydride on modified graphene: a first-principles study. J Phys Chem C 2017;121(34):18401–11.